



Regolith production and chemical weathering of granitic rocks in central Chile



Mercedes Vázquez^{a,*}, Sebastián Ramírez^a, Diego Morata^a, Martin Reich^a,
Jean-Jacques Braun^{b,c}, Sebastien Carretier^{a,b}

^a Department of Geology and Andean Geothermal Center of Excellence (CEGA), Facultad de Ciencias Físicas y Matemáticas, Universidad de Chile, Santiago, Chile

^b Géosciences Environnement Toulouse (Université de Toulouse, CNRS, IRD), 14 avenue Edouard Belin, 31400 Toulouse, France

^c Institut de Recherches Géologiques et Minières/Centre de Recherches Hydrologiques, BP 4110, Yaoundé, Cameroon

ARTICLE INFO

Article history:

Received 9 December 2015

Received in revised form 15 September 2016

Accepted 19 September 2016

Available online 26 September 2016

Keywords:

Critical zone

Central Chile

Chemical weathering

Cosmogenic beryllium

Geomorphology

ABSTRACT

We have evaluated the long-term chemical and physical weathering mass balance of an anomalously thick saprolite profile (>30 m thickness) developed in granitic rocks near Curacaví, Coastal Range of central Chile. The results of geochemical mass balance calculations for the regolith profile point to a moderate depletion for Na and Sr due to the plagioclase dissolution and precipitation of kaolinite. Furthermore, silicon shows a predominantly constant behaviour along the profile that is indicative of incongruent weathering of plagioclase, strongly suggesting that quartz dissolution conditions are not reached. In addition, low depletion of K, Mg, Ca, Rb, and Ba in the saprolite indicates a low degree of K-feldspar, biotite and hornblende weathering. Denudation rates calculated using cosmogenic ¹⁰Be data range from 20 to 70 m/Ma. If the saprolite thickness has reached a steady-state condition, the reported denudation rates lead to mineral residence times in the upper part of the saprolite profile of about 0.5 to 1.8 Ma. With such duration a higher weathering degree than observed at Curacaví would be expected. This apparent contradiction might be explained if all of the weatherable plagioclase has been dissolved under the present-day precipitation and temperature conditions of the Curacaví region. Therefore, we propose that the Curacaví profile could be in local equilibrium with respect to the weatherable fraction of plagioclase. A local equilibrium regime may be reached when the overall degree of depletion is small in a weathering profile. Uniform elemental distribution and low weathering degree in the thick weathering profile at Curacaví defy the traditional notion of weathering regimes and reveal the importance of exploratory studies in order to better understand weathering process in Mediterranean and semi-arid climate regions.

© 2016 Elsevier B.V. All rights reserved.

1. Introduction

Weathering is one of the most fundamental geological processes operating at the Earth surface, shaping landscapes, determining nutrient supply to ecosystems and regulating global chemical cycles. Silicate chemical weathering, in particular, may act as a key component in the long-term regulation of atmospheric CO₂ levels (Beaulieu et al., 2012) and hence modulates the global climate over the scales of millions of years (Walker et al., 1981; Kump et al., 2000).

The development of weathering profiles in rocks has been modelled using reactive transport algorithms and mineralogical and bulk geochemical measurements. These models take into consideration areas with “steady-state” regolith production rates, and erosion rates that are constant. The condition of steady-state system occurs when the

rate of descent of the limit between regolith and parent rock (weathering front), and the limit between regolith and soil/soil-air limit (denudation rate) are equal. Recently, Lebedeva et al. (2010) proposed two quantitative weathering models, i.e., a local equilibrium limit and a kinetic limit. The local-equilibrium condition is characterized by complete depletion of albite (Na-plagioclase) in the saprolite, while the kinetically limited condition is characterized by a gradient in plagioclase concentration from the top of the profile to some greater depth where the concentration approaches the concentration in bedrock.

The effects of the weathering process on bulk chemical and mineral distributions through weathering profiles have been extensively studied (Nesbitt, 1979; Middelburg et al., 1988; Burkins et al., 1999; Turner et al., 2003; Kamei et al., 2012). However, there is still a limited set of well-documented case studies that integrate denudation rate data, mineralogical observations and geochemical characterizations. Hence, there are few places where the weathering scenarios can be checked within the context of the balance between chemical depletion of minerals in the profile and their removal at surface by physical erosion.

* Corresponding author at: Departamento de Didáctica de Ciencias Experimentales, Universidad de Granada, Campus Universitario de Ceuta, Calle Cortadura del Valle, s/n, Ceuta, Spain.

E-mail address: mvazquez@ing.uchile.cl (M. Vázquez).

In this study we provide a comprehensive dataset that is aimed at unraveling the weathering regime involved in the development of a thick (>30 m) weathering profile developed in a granitic terrain in central Chile under semi-arid to Mediterranean climate conditions (Fig. 1). The low precipitation (100–400 mm/yr) and the mountainous context of the studied area are not favourable for developing thick regolith profiles. So this thick saprolite profile offers a unique opportunity to check the limiting factors that control soil profile formation. In order to tackle this issue, we combined cosmogenic ^{10}Be concentrations with geochemical and mineralogical data to quantify the denudation rates, the compositional variations and the degree of weathering of this saprolite along the profile. Detailed discussion of mineral, element and cosmogenic variations on Curacavi saprolite profile and their implication on weathering regime are presented. Traditional models of weathering

predict limited cases of elemental distribution along weathering profiles. This paper aims to contribute to improve the empirical framework normally used to build predictive weathering models.

2. Geological, morphological and climatic setting

Five trench-parallel continental morpho-structural units can be recognized from west to east in central Chile: Coastal Cordillera, Central Depression and Principal Cordillera, Frontal Cordillera, and Foreland (Fig. 1). The Coastal Cordillera is the oldest and westernmost belt comprising the remnants of a magmatic arc formed at the onset of the modern Andean subduction. The western domain of the Coastal Cordillera is formed by a Paleozoic–Jurassic metamorphic and intrusive basement covered by Late Miocene to recent marine deposits (Wall et al., 1996).

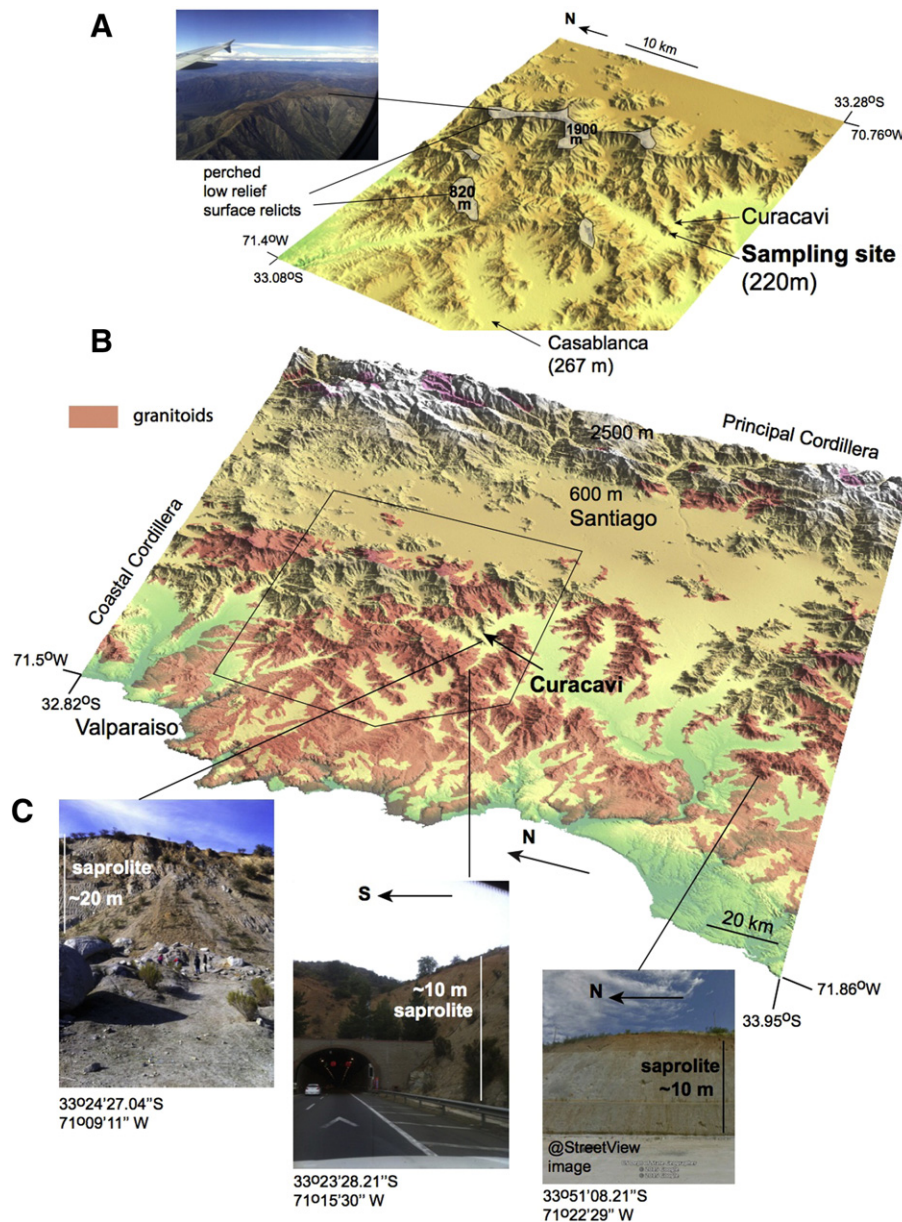


Fig. 1. A- Digital elevation model around the sampling location within the Coastal Cordillera near Curacavi, central Chile. The sampling site at Curacavi is located in a small butte-tremoin. This mountainous region is characterized by wide valleys and gentle to steep slopes flanking low relief surfaces perched between 900 and 2000 m a.s.l. These surfaces have been interpreted as relicts belonging to a peneplain developed before the Late Miocene (Borde, 1966; Farias et al., 2008). Based on these relict surfaces, the topography of the Coastal Cordillera has been interpreted as mainly relaxing for ~10 Ma, with the exception of a Plio-Pleistocene uplift of the westernmost part of the Coastal Cordillera (Farias et al., 2008). The picture on the left side shows the peneplain surfaces from the air. B- A more regional look. The sampling area (black polygon) is located in the Coastal Cordillera, dominated by granitoids. C- Photos show the sampled saprolite (on the left) and two other examples. Ten to twenty meters saprolites developed over granitoids rocks are ubiquitous observation in this region. The photo on the left is a quarry. The striae on the upper left of this image are due to erosion.

In contrast, the eastern domain is constituted of Jurassic–Cretaceous granites and late Jurassic to late Cretaceous volcanoclastic sequences.

The Jurassic–Cretaceous plutons in Coastal Cordillera were emplaced into the Paleozoic basement during a period of rifting. Rifting was associated with trench retreat caused by a period of slow South Atlantic sea-floor spreading (Larson and Pitman, 1972; Pankhurst et al., 1988; Aguirre et al., 1999). The development of the Coastal Cordillera marked the initiation of eastward subduction in the Early Jurassic, and the resultant evolution of the Central Depression (in central Chile) from a rift to a back-arc setting (Pichowiak, 1994). Rift closure as a result of the resumption of compression led to the cessation of the Coastal Cordillera arc magmatic activity in the Early Cretaceous (Parada et al., 2005; Scheuber and González, 1999). Important changes in the deformation regime of the Coastal Cordillera fore arc took place in the Late Cretaceous (80–60 Ma) as a result of the resumption of compression, rift closure, arc uplift, exhumation, eastward migration of magmatic arc activity towards Principal Cordillera, and thermal relaxation (Juez-Larré et al., 2010).

Remnants of low relief surfaces have been observed in the highest summits in eastern Coastal Cordillera (Fig. 1), showing evidences of relict continental erosion surfaces (Brüggen, 1950; Borde, 1966). The high altitude erosion surfaces are developed over Cretaceous intrusive bodies. Neither sediments nor volcanic deposits covering these surfaces have been reported. Smaller-scale erosion surfaces occur at lower elevations, and have been interpreted as relicts of a regional peneplain (Farias et al., 2008). Based on geomorphological and thermochronological arguments, Farias et al. (2008) proposed a landscape evolution scenario that involves uplift of the initial peneplain to elevations of 1.5–2 km a.s.l. at 10.5–4.6 Ma in the Curacaví area. The erosional response to this uplift was characterized by the retreat of sharp river knickpoints and the progressive widening of valleys and decaying of the relief. Towards the coast at ~35°S, the Navidad Formation constitutes the floor of Pleistocene marine terraces (Wall et al., 1996), and the present-day elevation of these surfaces represents a surface uplift of ~400 m. Encinas et al. (2006) described a 2.7 Ma lahar locally covering these terraces, which indicates that uplift occurred before 2.7 Ma (Farias et al., 2008).

From a geomorphological point of view, the present-day landscape of the Coastal Cordillera in central Chile corresponds to a mature relief. The altitude in the Coastal Cordillera diminishes progressively from highest elevations at 2100 m a.s.l. (at 33°S) to 1000 m a.s.l. (at 35°S). The main rivers are characterized by a minor channel slope and by an alluvial bed. Bedrock rivers are restricted to a 20 to 40 km-wide belt adjacent to the coastline in the western Coastal Cordillera, evidencing the recent surface uplift of this region (Farias et al., 2008).

The present-day climate developed in central Chile is controlled by the high topography of the Central Andes, with summit elevations reaching almost 7000 m a.s.l. (e.g., Aconcagua Mount) that efficiently block moisture coming from the east (Garreaud, 2009). Additionally, the upwelling of the cold Humboldt Current generates climatic inversions and thus prevents convection of moist air masses. The presence of the Pacific Ocean towards the west set Mediterranean (or dry-summer) climate conditions characterized by an average annual rainfall of 379 mm/yr at Curacaví (National Irrigation Commission, 1998), with a dry season lasting an average of 7 months. The average annual temperature is 16 °C that fluctuates between 3.3 and 27.4 °C.

Regolith profiles in this region are developed over andesitic volcanic rocks and granitic intrusives (Casanova et al., 2013). Soils developed over granodioritic rocks similar to those observed in the sampling site at Curacaví usually show a 10 cm-thick A horizon, and a B horizon which is typically 20–50 cm thick. Below, a thick saprolite of 10 to >30 m is observed regionally (Fig. 1).

3. Materials and methods

3.1. Sampling

Saprolite samples developed over granitic rocks were collected in the mouth of the Puangue river valley near Curacaví (Fig. 2). Samples were collected from top to bottom along a steep 33 m-thick weathering profile, using climbing equipment. Nineteen samples were collected every 2 m along the profile. For each sample, saprolite material was collected 5 cm below the surface of the exposed wall. Bedrock was not reached on the weathering profile and the depth to bedrock is

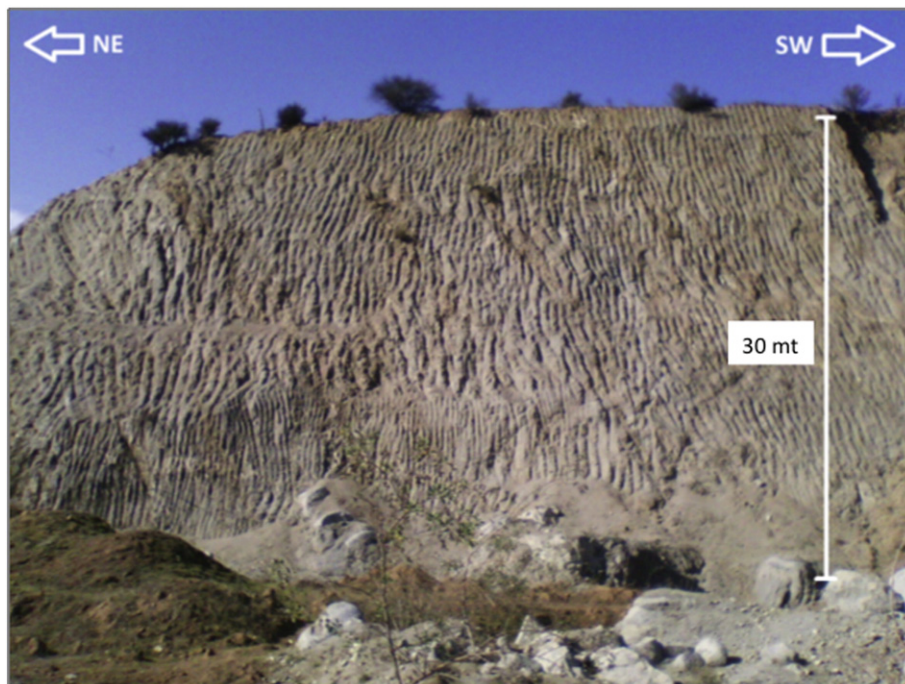


Fig. 2. Saprolite profile developed on granitic rocks in the Curacaví area. Samples were retrieved every 2 m along the profile using climbing equipment. Saprolite was highly friable, easy excavated with a shovel material and it has the same texture and structure of the bedrock.

Table 1
Bulk chemical analyses for major (SiO₂ to P₂O₅, wt.%) and trace (S to W, ppm) elements of saprolite and parent rock samples. DL = minimum.

Sample	Saprolite																			Bedrock					
	1	2	3	4	5	6	7	8	9	10	11	12	13	14	15	16	17	18	19	CUR7	SR1	SR2	SR3	SR4	SR5
Depth (m)	0	2,3	4,8	6,8	9,1	10,7	12,9	14,3	15,5	18,8	20,5	22,3	23,8	25,1	26,8	28,3	29,8	31,7	33,3						
SiO ₂	57,29	56,73	57,55	58,02	57,52	57,47	58,30	57,83	53,87	58,42	58,05	58,01	57,90	54,75	56,12	57,47	58,54	58,35	59,83	60,17	58,06	58,36	58,02	58,67	57,76
DL:0.01																									
Al ₂ O ₃	17,26	15,75	16,52	16,03	16,65	15,81	15,99	15,35	17,13	15,81	16,12	16,25	16,44	16,77	16,50	15,51	16,00	16,23	16,27	16,46	16,33	16,52	15,91	16,28	16,55
DL:0.01																									
Fe ₂ O ₃	7,08	7,86	7,01	6,49	6,43	7,09	6,68	7,21	8,06	6,74	6,54	6,69	6,81	7,77	7,64	7,44	6,65	6,58	5,86	5,99	7,03	6,65	7,25	6,56	6,61
DL:0.01																									
MnO	0,16	0,22	0,19	0,17	0,18	0,22	0,16	0,20	0,22	0,14	0,15	0,14	0,18	0,17	0,15	0,16	0,15	0,15	0,14	0,12	0,17	0,17	0,16	0,20	0,19
DL:0.01																									
MgO	2,69	3,02	2,68	2,83	2,99	3,18	2,77	3,10	3,32	2,99	3,01	3,23	2,82	3,58	3,20	3,19	2,98	2,73	2,68	2,83	3,34	3,30	3,42	3,40	3,49
DL:0.01																									
CaO	5,88	5,99	5,89	5,54	5,69	5,46	6,53	6,16	7,83	6,23	6,55	6,40	6,47	6,98	6,94	6,29	5,74	5,95	5,29	6,61	6,88	7,12	7,02	6,15	6,12
DL:0.03																									
Na ₂ O	2,31	2,26	2,55	2,78	2,50	2,53	2,55	2,34	2,66	2,53	2,60	2,49	2,68	2,56	2,55	2,24	2,46	2,65	3,05	3,00	2,94	3,12	2,73	3,28	3,12
DL:0.08																									
K ₂ O	2,96	2,58	3,18	3,36	3,08	3,37	2,93	2,97	2,20	3,05	2,86	2,30	2,40	2,45	2,26	3,18	3,17	3,40	3,41	3,23	2,48	2,31	2,82	2,88	3,16
DL:0.01																									
TiO ₂	0,95	1,16	0,94	0,87	0,81	0,87	0,88	1,04	0,98	0,95	0,90	0,96	0,94	1,05	1,02	1,12	0,95	0,93	0,78	0,73	0,92	0,78	0,98	0,77	0,90
DL:0.02																									
P ₂ O ₅	0,18	0,27	0,20	0,22	0,19	0,20	0,22	0,20	0,52	0,22	0,21	0,18	0,19	0,21	0,20	0,22	0,20	0,21	0,19	0,20	0,22	0,21	0,25	0,21	0,25
DL:0.01																									
LOI	3,02	3,95	3,09	3,50	3,72	3,55	2,67	3,33	2,95	2,72	2,75	3,14	2,91	3,44	3,13	2,95	2,94	2,56	2,29	0,39	1,36	1,19	1,15	1,38	1,59
Total	99,77	99,78	99,80	99,79	99,76	99,76	99,70	99,72	99,73	99,79	99,74	99,79	99,76	99,73	99,71	99,76	99,78	99,74	99,79	99,74	99,73	99,74	99,72	99,77	99,72
CIA (%)	49,4	47,5	47,4	46,7	48,3	47,1	45,4	45,7	44,9	45,7	45,5	47,1	46,7	46,2	46,1	45,5	47,2	46,3	47,0	44,6	44,9	44,5	43,9	45,3	45,7
S DL:0.05	49	<DL	37	41	60	47	43	<DL	<DL	30	38	35	36	54	34	34	44	45	39	65	53	46	54	42	47
Cl DL:82.12	485	454	515	436	490	451	659	608	508	486	608	575	607	552	515	496	498	502	458	691	711	770	685	529	548
V DL:0.81	156	<DL	<DL	<DL	170	172	160	196	143	<DL	159	159	183	185	205	<DL	<DL	138	<DL	152	180	<DL	<DL	<DL	161
Co DL:0.680	14	17	13	25	5	<DL	11	<DL	21	23	36	17	25	32	<DL	19	29	8	20	17	29	26	18	<DL	26
Ni DL:0.30	<DL	<DL	21	17	18	22	21	<DL	<DL	31	25	14	21	25	24	28	28	24	<DL	<DL	24	25	29	26	32
Cu DL:2.39	84	64	65	70	75	84	117	70	313	114	91	39	51	72	174	82	139	161	106	48	108	217	205	93	114
Zn DL:0.95	97	128	104	85	107	100	103	119	149	89	88	81	96	101	105	116	95	109	86	67	106	91	96	110	106
Ga DL:2.56	21	16	18	15	22	18	18	21	<DL	21	18	16	<DL	17	21	21	18	19	11	18	21	17	19	18	21
Rb DL:0.13	123	107	128	137	119	140	115	119	105	127	116	112	98	119	114	142	134	151	141	128	96	80	104	104	123
Sr DL:6.42	345	380	369	359	391	351	414	400	513	340	360	353	376	390	439	379	351	363	336	315	392	400	404	379	381
Y DL:1.95	23	23	22	21	23	18	20	17	17	26	24	17	21	26	29	15	22	20	24	18	25	23	24	23	22
Zr DL:12.57	166	150	139	162	128	135	146	148	210	155	153	157	158	135	141	196	224	220	186	145	158	157	199	160	175
Ba DL:0.81	388	340	434	453	414	507	530	597	311	423	398	290	367	334	402	508	400	461	435	446	362	477	372	431	444

Table 2

Average content of major and trace elements of saprolite and parent rock samples.

	SiO ₂ (%)	Al ₂ O ₃ (%)	Fe ₂ O ₃ (%)	MnO (%)	MgO (%)	CaO (%)	Na ₂ O (%)	K ₂ O (%)	TiO ₂ (%)	P ₂ O ₅ (%)	LOI (%)	S ppm	Cl ppm	V ppm	Co ppm	Ni ppm	Cu ppm	Zn ppm	Ga ppm	Rb ppm	Sr ppm	Y ppm	Zr ppm	Ba ppm
Saprolite	57,46	16,22	6,96	0,17	2,99	6,17	2,54	2,87	0,95	0,22	3,06	40	517	167	17	22	91	101	18	122	377	21	161	413
Bedrock	58,50	16,34	6,67	0,17	3,29	6,64	3,03	2,79	0,84	0,22	1,08	50	649	163	22	27	116	94	18	104	377	22	164	419

unknown. Despite this limitation, six samples of fresh bedrock were obtained from nearby outcrops within the catchment.

3.2. Bedrock/saprolite geochemistry and mineralogy

The mineralogy of 26 powdered samples was determined by X-ray diffraction (XRD) at Crystallography and X-Ray Diffraction Laboratory, Department of Physics, FCFM, Universidad de Chile using a Bruker D8 Advanced diffractometer with Cu-K α radiation and Bragg–Brentano geometry. The analytical parameters were: acceleration voltage of 40 kV, a beam current of 20 mA, a counting time of 52.07 s/step, and a scan speed of 0.02°/s. Thin sections of granitic rocks and regolith samples were prepared for observation using optical petrography and scanning electron microscopy (SEM) techniques at the Andean Geothermal Center of Excellence (CEGA), FCFM, Universidad de Chile (FEI Quanta 250, with an accelerating voltage of 4–15 kV, a beam current of 1–2 nA and a counting time of 50 s).

Bulk chemical analyses were carried out on 26 samples at the Instituto Andaluz de Ciencias de la Tierra, CSIC-Universidad de Granada. A Wavelength Dispersive X-Ray Fluorescence Spectrometry (WDXRF; Bruker AXS S4 Pioneer with an Rh anode X-ray tube) with an analytical detection limit of 0.1% and an instrumental error < 1% was used. Concentrations of Si, Al, Ca, Fe, Na, K, Ti, and other major rock-forming elements were measured from homogeneous glass disks, while concentrations of Zr and other trace elements were measured from pressed powdered samples.

3.3. Cosmogenic nuclide analysis

The chemical composition of soil and regolith depends on the rate of removal of the surface (physical erosion rate) and thus is linked to the total denudation rate (chemical + physical) (e.g. Riebe et al., 2003).

In order to quantify the denudation rate, we used ¹⁰Be concentrations in three saprolite samples taken at different depths between 1 and 5.8 m below the top of the weathering profile. We assumed that the surface erosion has occurred for several Myrs, without in situ ¹⁰Be

inheritance, with a constant density, so that the ¹⁰Be concentration C(z) has reached a steady-state condition following this equation (e.g. Lal, 1991; Braucher et al., 2003):

$$C(z) = \frac{P_0 x_1}{\rho D + \Lambda_n} \cdot e^{-\frac{z}{\Lambda_n}} + \frac{P_0 x_2}{\rho D + \Lambda_{\mu s}} \cdot e^{-\frac{z}{\Lambda_{\mu s}}} + \frac{P_0 x_3}{\rho D + \Lambda_{\mu f}} \cdot e^{-\frac{z}{\Lambda_{\mu f}}} \quad (1)$$

where z is the depth, D is the denudation rate, $\Lambda_n = 160 \text{ g/cm}^2$, $\Lambda_{\mu s} = 1500 \text{ g/cm}^2$, $\Lambda_{\mu f} = 5300 \text{ g/cm}^2$ are the attenuation lengths for neutrons, slow and fast muons, respectively, $x_1 = 97.85\%$, $x_2 = 1.5\%$, $x_3 = 0.65\%$ are the relative contributions of these particles to the ¹⁰Be surface production rate P_0 [at/g/yr] (Braucher et al., 2003). The radioactive decay constant of ¹⁰Be (λ) is $4.99 \cdot 10^{-7} \text{ yr}^{-1}$ (Chmeleff et al., 2009). $P_0 = 4.73 \text{ at/g/yr}$ calculated from Stone (2000) at the sampling latitude and elevation.

In order to determine a best-fit denudation rate, we minimise the χ_2 value defined by

$$\chi_2 = \sum_{i=1}^{i=3} \left[\frac{C_i - C(z)}{\sigma} \right]^2$$

where C_i is the ¹⁰Be concentration of a sample I at depth, σ the ¹⁰Be concentration uncertainty and C(z) given by Eq. (1).

The ¹⁰Be concentrations were obtained by the ASTER team using accelerator mass spectrometry (AMS) at the Centre de Recherche et d'Enseignement de Géosciences de l'Environnement (CEREGE), Aix en Provence, France, according to methodologies described in Arnold et al. (2010).

4. Results

4.1. Chemical and mineralogical analysis

Tables 1, 2 and 3 show the bulk analyses of major and trace elements of the saprolite and parent rock, and the mineralogical composition

Table 3

XRD patterns for the composite samples. Key for XRD analysis: empty cell: absence, x: presence (<10%), xx: abundant (10–35%) and xxx: very abundant (>35%).

Sample	Depth	Quartz	Plagioclase	Oligoclase	Biotite	Horblende	Kaolinite	Clays 2:1	Chlorite
1	0.6	XX	XX	X	XX	XX	XX	X	
2	2.9	XX	XXX	X	X	XX	X	XX	
3	5.4	XX	XXX	X	X	XX	XX	XX	
5	7.4	XX	XX	X	X	XX	XX	X	
5	9.7	XX	XX	X	X	XX	XX	XX	
6	11.3	XX	XX	X	XX	XX	XX	X	
7	13.5	XX	XX	X	XX	XX	X	X	
8	14.9	XX	XXX	X	X	XX	XX	X	
9	16.1	XX	XXX	X	XX	XX	XX	X	
10	19.4	XX	XX	X	XX	XX	XX	X	
11	21.1	XX	XX	X	X	XX	X	X	
12	22.9	XX	XXX	X	X	XX	X	X	
13	24.4	XX	XXX	X	XX	XX	X	X	
14	25.7	XX	XXX	X	X	XX	X	X	
15	27.4	XX	XXX	X	XX	XX	X	X	
16	28.9	XX	XXX	X	X	XX	X	X	
17	30.4	XX	XXX	X	X	XX	X	X	
18	32.3	XX	XXX	X	X	XX	X	X	
19	33.9	XX	XXX	X	XX	XX	X	X	
SR-3	–	XX	XXX	X	X	XX			X

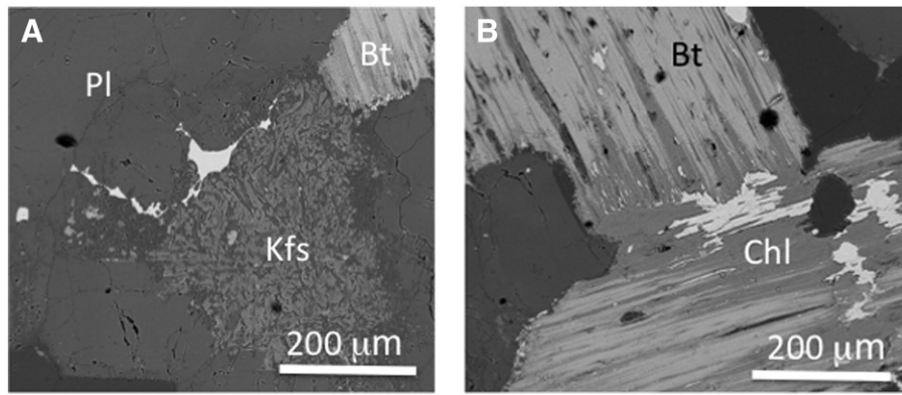


Fig. 3. SEM back-scattered electron images (BSE) of fresh granitic rocks. (A) Primary minerals are K-feldspars (Kfs), plagioclase (Pl) and biotite (Bt). K-feldspars and plagioclase appear as intergrowths. (B) Topotactic replacement of biotite crystals by chlorite (Chl), showing a fanned-out texture.

determined by XRD, respectively. Combined XRD patterns and SEM–EDX analyses indicate that the major minerals of fresh granitic rocks are quartz, oligoclase (An19), K-feldspar, biotite, hornblende and chlorite (Fig. 3). Accessory minerals are zircon, apatite and magnetite. Chloritization of biotite crystals are frequently observed in the parent rock (Fig. 3B). Zircon occurrence is usually associated with the presence of biotite. The average parent rock is an oligoclase-quartz rich tonalite. Average compositions of the major and trace elements are shown in Table 2. Barium, Sr, Rb, Cl, Cu and S present the highest concentrations (Table 1). Certain trace elements such as Cr, As, Br, I and W are generally below the detection limit.

Clay minerals are present in the saprolite (Table 2), and kaolinite is abundant from the top profile to 19.4 m in depth. Significant contents of smectite or vermiculite were detected in some samples (samples 2, 3 and 6). Gibbsite, hematite, goethite are absent in the bulk XRD patterns meaning that, if present, their abundance is <5%. Back-scattered electron (BSE) images reveal that quartz is almost unaffected by alteration and that feldspars undergo important alteration (Fig. 4). Dissolution features of plagioclase can be observed, including solution etch pits similar to those described by Berner and Holdren (1977, 1979) for natural and experimentally-dissolved feldspar. Pits are developed along cleavage planes. Energy dispersive X-ray spectrometry (EDS) analyses indicate the presence of kaolinite filling voids in plagioclase. Although almost unweathered grains of biotite can be observed (with no visible textural changes), most of biotite grains show EDS spectra with lower Si and Mg and higher Ca content than a pure biotite, suggesting cryptic alteration to smectite or vermiculite.

Tables 1 and 2 show the bulk chemical composition of saprolite. The most abundant trace elements are Ba; Zr; Sr; Rb; Zn; Cu; Cl. Some trace elements (Cr, As, Br, I and W) are generally below the detection limit of XRF, and we did not consider these elements in further interpretations. Depth-profiles for selected elements in the saprolite are showed in Fig. 5.

4.2. ^{10}Be -derived soil denudation rate

Fig. 6A shows modelled ^{10}Be concentration profiles for different saprolite bulk densities (ρ) and denudation rates. A problem during the sampling did not allow us to estimate ρ with accuracy. Furthermore, we acknowledge that depth and time variations in ρ can change the ^{10}Be concentration predicted by Eq. (1). (Rodés et al., 2011). Thus, we tested the effect of two different granitoid densities of 2.1 g/cm³ and 2.7 g/cm³. The corresponding best-fit denudation rates are 62 and 42 m/Ma, respectively. Given the small number of data, we also illustrate other modelled profiles using denudation rates between 20 and 72 m/Ma. Fig. 6A shows that these models bracket the data.

We also considered possible anthropogenic erosion, given that the B horizon appears less thick than in another outcrops that are distant

50 m from the sampling site. A 40 cm recent removal improves slightly the fit and changes the best-fit denudation rates to 30 and 48 m/Ma (Fig. 6B). Models using D between 20 and 58 m/Ma bracket the data. The similar ^{10}Be concentration at 2.9 and 5.4 m and the associated misfit

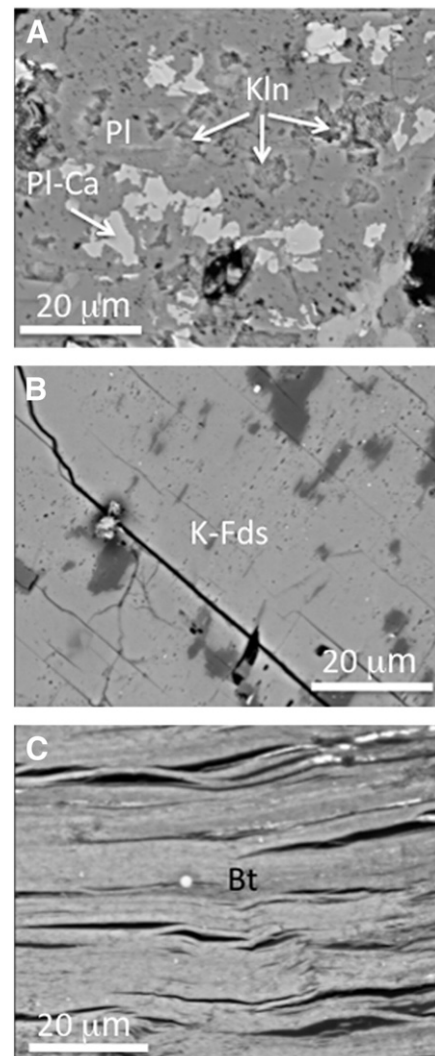


Fig. 4. SEM-BSE images of saprolite samples. (A) Plagioclases (Pl) show crystallographic controlled dissolution. Etch pits are filled by layers of kaolinite (Kln). The pseudomorph could have acted as a protective layer and inhibited plagioclase dissolution. (B) Almost unweathered K-feldspar with etch pits free of secondary minerals. (C) Biotite (Bt) crystal, without significant evidences of weathering.

may correspond to the inheritance of an older period with lower denudation rate (the deeper tail of a previous exponential ^{10}Be concentration profile). Exploring more complex scenarios than the steady-state assumed here requires more data. Overall, we thus estimate a conservative denudation rate ranging between 20 and 72 m/Ma.

5. Discussion

In this section we address the quantification of the chemical changes within the regolith using appropriate immobile element and parent

rock references, in order to constrain the weathering regime. We assume equilibrium between regolith production rate and surface erosion rate, from which we calculate a regolith production rate from ^{10}Be concentrations (Table 4).

5.1. Long-term elemental fluxes in the saprolite

Long-term elemental fluxes have been typically inferred using a mass balance approach (April et al., 1986; Brimhall and Dietrich, 1987). The depletion or enrichment of the element j moving in or out

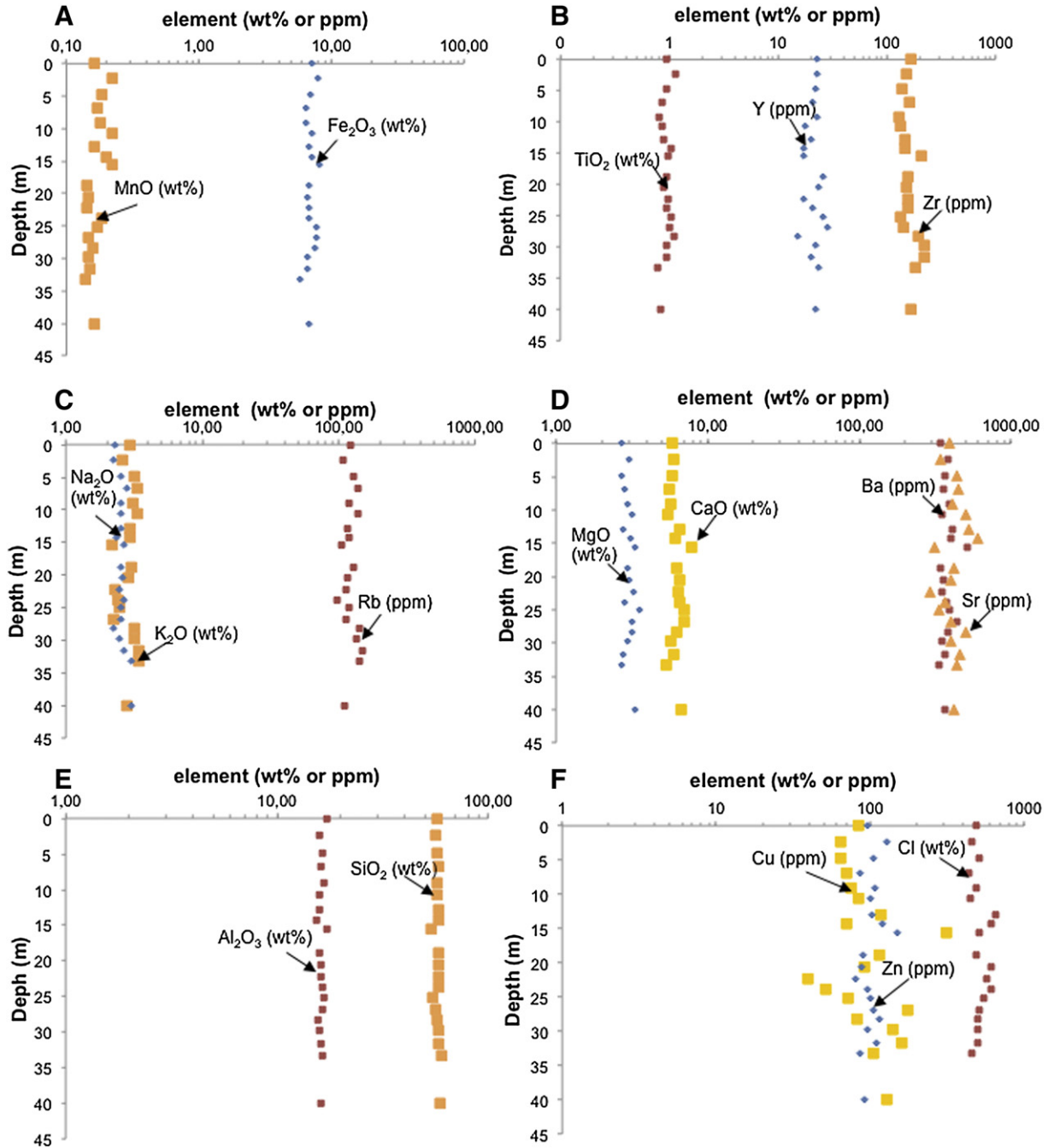


Fig. 5. Depth-profiles for selected elements in the saprolite: redox-sensitive (Fe and Mn), potentially immobile (Zr, Y and Ti), potentially mobile as alkaline (Na, K, Rb), alkaline earths (Ca, Mg, Sr, and Ba), Si, Al, Cl and heavy metals (Cu and Zn). Na shows a slightly depletion trend along the profile. K, Rb, Mg, Ca and Ba show a not pattern, rather the concentrations are constant along depth. Ba shows a general depletion trend along the profile. Fe and Mn show slight enrichment trends. Si, Al and Y show less obvious trends. Cu and Zn present a notorious depletion (from 26 to 22 m and from 15 m until surface), and enrichment trends (from 22 to 25 m). Among the immobile elements, Ti shows a constant trend along the profile. However, zirconium shows a general depletion trend, except between 33 and 29 m and between 5 m and profile surface, where Zr contents increase.

the system is determined using the elements-mass-transfer coefficient ($\tau_{j,w}$) given by:

$$\tau_{j,w} = \frac{C_{j,w}}{C_{j,p}} \frac{C_{i,p}}{C_{i,w}} - 1 \quad (2)$$

where $C_{j,w}$ and $C_{j,p}$ are the chemical contents of the element j (in wt.%) in the regolith and in the parent rock, respectively. $C_{i,w}$ and $C_{i,p}$ are the concentrations for an immobile element in the regolith and in the parent rock. Enrichment occurs when the value of the $\tau_{j,w}$ is positive and reflects a mass gain in the element j of the weathered materials compared to the parent rock. In contrast, depletion occurs when the value of the $\tau_{j,w}$ is negative indicates a mass loss. If the $\tau_{j,w} = 0$, the element is immobile during weathering.

Mass balance calculations requires i) a precise assessment of the parent rock composition, prior to the chemical weathering onset, and ii) choosing an appropriate immobile element, which should be very insoluble and resistant to chemical weathering dissolution loss. In this particular case, and considering that the bedrock did not outcrop at the bottom of the weathering profile, the calculations were carried out using the average compositions of six representative rock samples collected from nearby outcrops (see Table 2).

The potentially elements immobile are Zr, Ti, Y, Hf, Th and Nb (Riebe et al., 2003; Braun et al., 2012). Due to their extremely low contents at Curacaví (always below detection limits), Hf, Th and Nb could not be used as immobile (inert) elements in our analysis. Titanium contents show minor dispersion ($\sigma \sim 10\%$, with respect to average Ti), while Y and Zr display standard deviations of about 17 and 18%, respectively. Among all potentially immobile elements, titanium shows the highest enrichment trend towards the topsoil. For these reasons, titanium was considered the best immobile (inert) element for mass balance calculations. Fig. 7 show the $\tau_{j,w}$ of the potentially immobile Zr and Y. The behaviour of Zr and Y is similar, showing a moderate depletion, with losses reaching 40% for Zr and 50% for Y.

Numerous studies have revealed that Zr and Ti present some degree of mobility (Sudom and St. Arnaud, 1971; Colin et al., 1993; Cornu et al., 1999; Kurtz et al., 2000; Taboada et al., 2006; Jin et al., 2010). Recently Bern et al. (2015) demonstrated that Ti and Zr elements are mobile only in the colloidal phase in a South African catena. The lack of enrichment trend of Zr in the Curacaví profile and its highest standard deviation might reflect some redistribution associated with the colloidal phase.

Field observations indicate that physical structure of parental rock is preserved, suggesting isovolumetric weathering. In addition, SEM images show that secondary minerals formed in the Curacaví saprolite are pseudomorph of the primary minerals and textural characteristic of parental rock is conserved (Fig. 4). Isovolometric weathering assumption allows us to calculate the average bulk density of the saprolite using a volumetric strain of zero (Braun et al., 2012). Thus, and by using the formula $\rho_{\text{saprolite}} = \rho_{\text{parent}} (C_{\text{Ti parent}} / C_{\text{Ti saprolite}})$ the average bulk density of the saprolite was calculated at 2.46 g/cm^3 .

5.2. Elemental mass transfer profiles

Mass balance calculations were undertaken for chosen elements, assuming isovolumetric weathering. In this case, $\text{CDF}_j = -\tau_j$, and therefore, $\tau_j = -1$ indicates a CDF_j of 100% for the j element.

Fig. 8 displays the mobility of alkaline and alkaline earths. $\tau_{j,w}$ values show practically an uniform trend along all the profile depth, which deeply contrast with the data in the literature. Most published works present enrichment or depletion gradients of $\tau_{j,w}$ values along the depth profile (e.g. Braun et al., 2012; White et al., 1998). Curacaví profile show that Ca and Mg display a significant depletion behaviour (up to 35% mass loss). Sodium shows a significant depletion trend, (up to 45% mass loss). The behaviour of K does not show a clear trend, and

most of the samples have K concentrations within the variability ranges of the parental (unaltered) granitic rock.

The semi-quantitative SEM-EDS analyses of plagioclase show compositions varying between 81% albite and 19% anorthite (mostly oligoclase). SEM observations show that the Na-plagioclase (oligoclase) crystals could have suffered crystallographically controlled dissolution. Presence of etch pits indicate that the dissolution process was mediated by a interface-limited mechanism, reflecting the site-selective nature of interfacial processes (Bernier, 1978, 1981; Brantley et al., 1986; Lasaga and Blum, 1986; Schott and Petit, 1987). These etch pits are completely filled by kaolinite. This is consistent with XRD data, where kaolinite is an abundant mineral phase in samples close to the surface of the profile. Oligoclase dissolution and precipitation of kaolinite could explain the depletion mainly of Na, and to lesser extent of Ca, described by the following reaction:

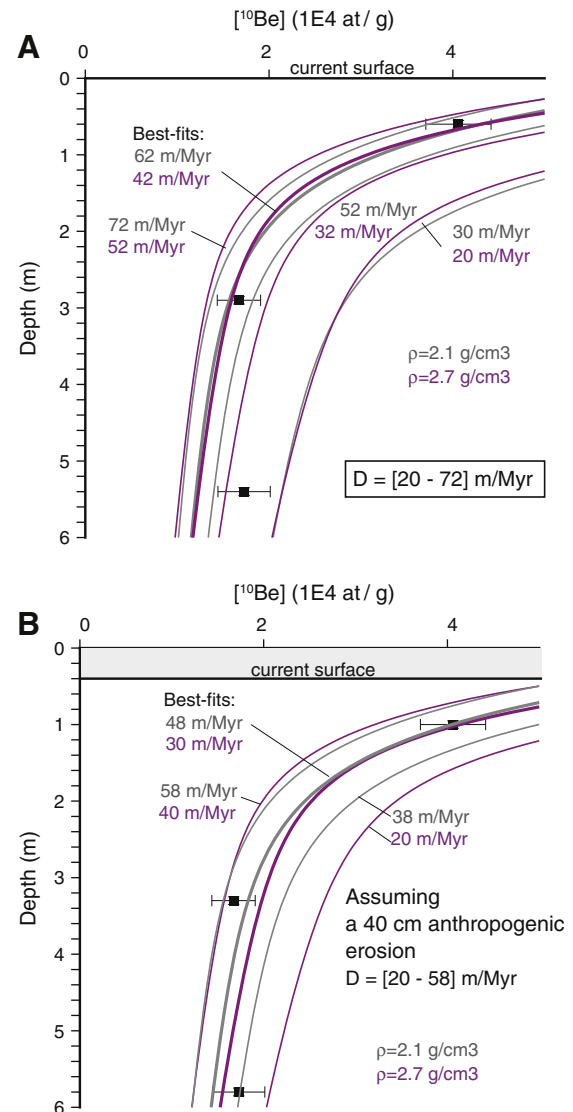
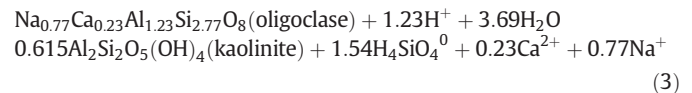


Fig. 6. Depth-profile models of ^{10}Be concentrations. (A) Best-fit profiles correspond to the denudation rates of 62 and 42 m/Myr, for two extreme saprolite density values. The other profiles bracket the samples ^{10}Be concentration uncertainties. (B) The same but assuming that 40 cm of soil have been eroded by humans in a recent past.

Table 4

Data corresponding to ¹⁰Be measurements at ASTER, Cerege, France.

Sample	Be-10/Be-9	Uncertainty Be-10/Be-9 (%)	Be-10/Be-9 corrected of chemical blank	Uncertainty Be-10/Be-9 corrected of chemical blank	Mass dissolved quartz q	Spike Be-9 at	Error Be-9 at	[Be-10] at/g	Uncertainty [Be-10] at/g
3	1,8846E-14	14,7176	1,7092E-14	2,8135E-15	20,1098	2,0339E+19	6,0547E+16	17,286	2846
2	1,9052E-14	12,5591	1,7298E-14	2,4388E-15	20,9685	2,0274E+19	6,03543E+16	16,725	2359
1	4,3146E-14	8,3085	4,1392E-14	3,6157E-15	20,8237	2,0432E+19	6,08231E+16	40,613	3550

Uncertainty Be10/Be9 (%): number of counts and standard uncertainty.

The previous reaction might also explain the similar behaviour of both Sr and Ca, because Ca²⁺ is frequently replaced by Sr²⁺ in plagioclase. SEM observations show that the zones that are richer in anorthite within the plagioclase crystals are the first to dissolve forming etch pits and later filled with kaolinite. Kaolinite fillings might act as a protective layers inhibiting the continued plagioclase dissolution process. Silicon shows a constant behaviour throughout the profile. This might indicate that plagioclase grains are not completely dissolved, and therefore the limiting conditions at which quartz is dissolved are not achieved in the Curacaví profile. Calcium and Mg show a similar trend along the profile, indicating low weathering of amphibole (hornblende) crystals. Potassium concentrations along the saprolite are similar to those of the parent rocks, indicating that the weathering of the K-feldspar and biotite is not significant. Potassium, Rb and Ba show similar trends, in agreement with the fact that K-feldspar and biotite are mostly stable phases during weathering (because Rb and Ba are able to substitute K in both minerals). K-feldspar crystals display evidence of weathering in certain samples (Fig. 4). However the K-feldspar modal abundance is significantly lower than that of plagioclase or hornblende. Therefore, the K amount related to K-feldspar dissolution contributes to a lesser extent to the K trend along the profile. In addition, the weathering rate of K-feldspar is significantly lower than for plagioclase (Nesbitt et al., 1980; Brantley and White, 2009). SEM observations show almost unweathered grains of biotite in the saprolite. In contrast, biotite-chlorite intergrowths were observed in parent rock samples. Chlorite appears between exfoliation planes of biotite, forming fanned-out textures, characteristics of topotactic replacement (Fig. 3B). However, chlorite is entirely absent in the saprolite phyllosilicates. Therefore, rapid breakdown of chlorite shall occur in the incipient weathering front, out of reach in the present study. Previously published experimental data suggests that Mg-rich chlorites have dissolution rates similar to biotites (May et al., 1995), but that Fe-rich chlorites such as present in parent

rocks studied, dissolve 2–3 orders of magnitude faster than biotite (Nagy, 1995).

5.3. Weathering regime

Chemical weathering of the saprolite is described by plagioclase weathering to kaolinite, showing significant Na depletion along the profile. Table 1 show the values obtained for Chemical Index of Alteration, CIA (Nesbitt and Young, 1982). CIA considers aluminium as a conservative element and reflects the extent of plagioclase and feldspar weathering, i.e., leaching of K, Na and Ca, and transformation into authigenic clay minerals, such as kaolinite. As weathering progresses, the CIA increases from about 50 for fresh rocks (granite, gneiss) to 100 for optimum weathering (for instance in lateritic profiles, see Braun et al., 2012). In our case, the CIA of the average parent rock is of 44.8% ± 0.6. The CIA of the saprolite is quite homogeneous, varying from 49.4% in more superficial samples to 47.0% in the profile bottom, reflecting a low chemical weathering grade.

Fig. 8 and Table 1 show that plagioclase grains are not completely weathered at the more superficial levels of the saprolite. We do not know if plagioclase crystals persist in the upper most soil layer, because the soil was not sampled at the top of the profile. However, the maximum CDF values of 27% and maximum Na depletion at 45% observed in the saprolite strongly suggest that it is unlikely that complete depletion of plagioclase occurred in the 20 cm of soil. Lebedeva et al. (2010) defined two opposite weathering regimes, a local equilibrium limit and a kinetic limit. The local-equilibrium case is characterized by complete depletion of albite in the saprolite. Whereas, the kinetic limit regime is characterized by a gradient in Na concentrations across depth, especially in elements-mass-transfer coefficient. Fig. 8 demonstrates that, in a strict sense, the Curacaví profile is neither kinetically limited

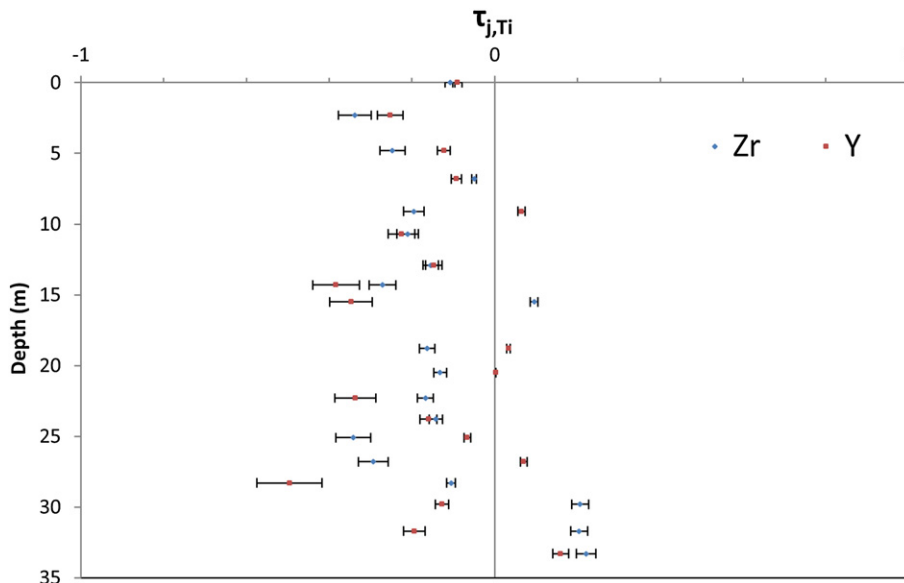


Fig. 7. Mass transfer function (τ_{jw}) for potentially other immobile elements (Zr and Y) versus depth. The compositional range of the parent material is shown by the rectangle.

nor in local equilibrium. Thus, our results differ from the weathering regime proposed from reactive transport simulations.

We propose that the Curacaví profile could be in a local-equilibrium condition, in which all the plagioclase that was accessible to weathering under the conditions of precipitation and temperature of the region has been dissolved. The pseudomorphs of kaolinite could act as a protective layer inhibiting continued plagioclase dissolution.

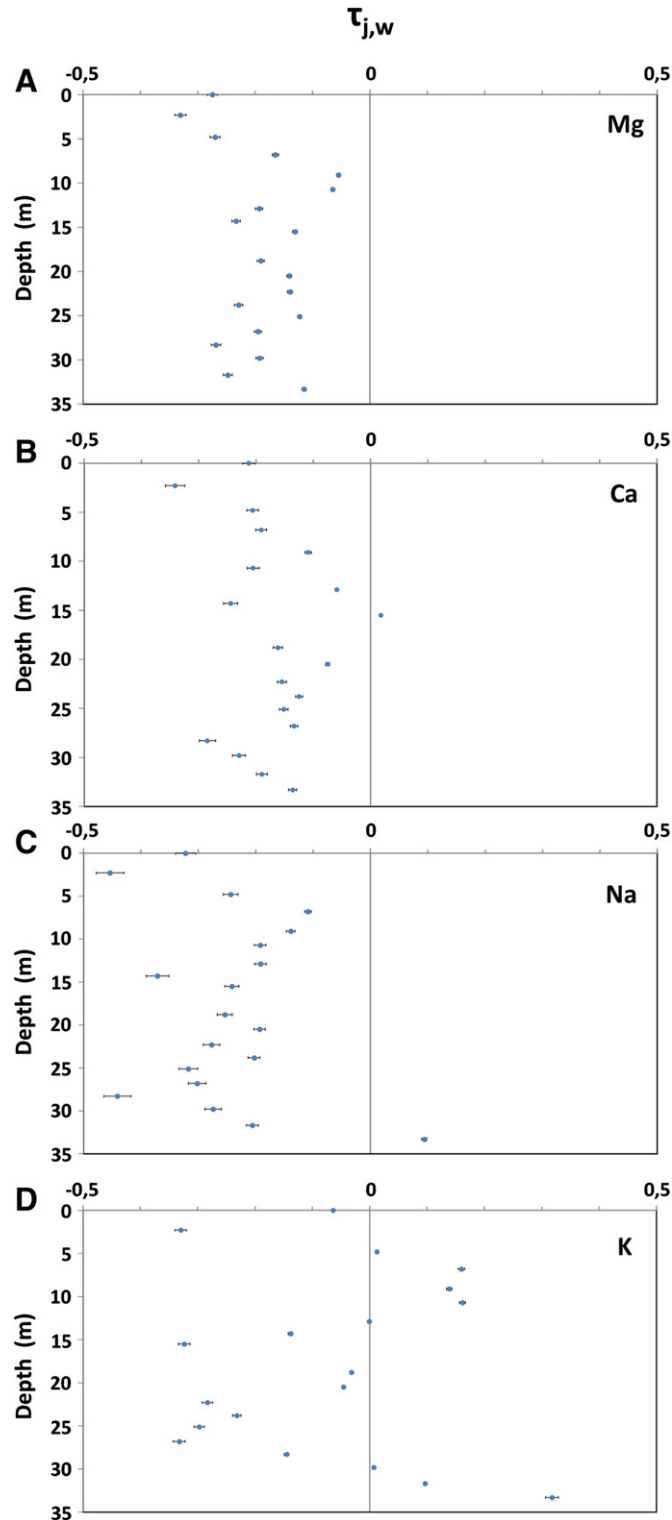


Fig. 8. Mass transfer function ($\tau_{j,w}$) for Mg (A), Ca (B), Na (C) and K (D) versus depth. The compositional range of the parent material is shown by the rectangle.

The extensive thickness of the studied regolith could be explained when advection-driven transport occurs and the Darcy hydraulic gradient is considerable, because the regolith thicknesses developed with only diffusive transport are too thin (Lebedeva et al., 2010). Bazilevskaya et al. (2013) demonstrate that when precipitation is higher than evapotranspiration, thick regolith profiles occur in Fe-poor granite. In this case, weathering cause fracturing around biotite. Biotite oxidation is often an early fracture inducing reaction that occurs deep in granite rock (Graham and Franco-Vizcaino, 1992; Graham et al., 1994; Fletcher et al., 2006; Buss et al., 2008). In this way, deep-water infiltration leads to the formation of a thick regolith profile. Therefore, our analysis strongly suggests that significant meteoric water circulation was necessary to sustain a local equilibrium with advective transport and produce an extensive regolith profile at Curacaví.

5.4. Chemical weathering rates under the equilibrium hypothesis

In a landscape subjected to constant climate and erosion conditions, a state of equilibrium between the total denudation rate (physical + chemical) and the rate of conversion from bedrock to weathered rock may be reached (Brimhall et al., 1991; Riebe et al., 2003). Note that this is not always the case, as for instance, a significant climatic shift would alter equilibrium and contradict this assumption (Riebe et al., 2003).

Within the frame of this equilibrium hypothesis, the quantification of chemical weathering rates is usually calculated using the Chemical Depletion Fraction (CDF) (Riebe et al., 2003), which is defined as the fraction of total denudation that is accounted for by chemical weathering.

$$CDF = \left(1 - \frac{(\text{inert element})_{\text{rock}}}{(\text{inert element})_{\text{weathered}}} \right) \quad (4)$$

where (inert element)_{rock} is the concentration of the immobile (inert) element in the parent rock and (inert element)_{weathered} is the concentration of the immobile (inert) element in the weathered material.

Using Ti as the inert element, the calculated average CDF for the Curacaví profile is 10.3%, reaching a maximum value of 26.9% on samples closer to surface of the profile. Furthermore, the denudation rates calculated using cosmogenic ^{10}Be data range from 20 to 70 m/Ma for the Curacaví profile. Therefore, if we assume equilibrium conditions, the chemical weathering rate is 2 to 7 m/Ma and the physical erosion is 18 to 63 m/Ma. This would indicate that around 10% of the mass loss in this particular system is due to chemical weathering flux. If the equilibrium hypothesis is right, our data would show that chemical weathering rates are low and physical erosion is the dominant factor. Furthermore, within the frame of this hypothesis (rock-to-saprolite conversion rate = ^{10}Be -derived denudation rate) a constant saprolite thickness of 33 m would imply that the maximum residence time of a mineral grain in the saprolite is between 0.5 and 1.8 Ma. This long residence time should favour the mineralogical depletion, which is not observed. We propose that the low depletion in the saprolite is due to a negative feedback of the kaolinite precipitation, which could protect feldspar grains from dissolution.

6. Conclusions

The Coastal Cordillera in Central Chile in the region of Santiago displays a thick saprolite of >10 m developed over granitoids. The weathering grade of the saprolite studied in Curacaví is very low. We proposed that this profile could be in local equilibrium with respect to the weatherable fraction of plagioclase. Plagioclase crystals are still present in saprolite after crystallographically controlled dissolution, and the developed etch pits were filled by kaolinite. Kaolinite crystals could have acted as a protective layer inhibiting more advanced plagioclase dissolution. Therefore, local equilibrium could be reached if the

overall degree of depletion is small and weatherable grains are still present in the saprolite. Understanding weathering processes in these profiles needs to focus on mineralogical and geochemical studies to improve the empirical framework for building better predictive models.

Acknowledgements

This research was supported by Chilean Research grants Fondecyt Regular 1140629 and Fondap-Conicyt 15090013 “Andean Geothermal Center of Excellence (CEGA)”. Additional support was provided by LMI COPEDIM and the Millennium Nucleus for Metal Tracing Along Subduction (NC130065). Authors thank to Felipe Ugalde, Francisco Hevia and David Valenzuela for their help with the sampling. We also thank to Dr. Francisca Martínez-Ruiz and Juan Santamarina for the use of XRF equipment at the Instituto Andaluz de Ciencias de la Tierra (CSIC-UGR), and Cristián Nievas from Department of Geology, Universidad de Chile, for his help with scanning electron microscopy (SEM) observations. We thank the ASTER team in Cerege for the cosmogenic measurements. We thank François Chabaux and two anonymous reviewers for the helpful comments which improved greatly this paper.

References

- Aguirre, L., Feraud, G., Morata, D., Vergara, M., Robinson, D., 1999. Time interval between volcanism and burial metamorphism and rate of basin subsidence in a Cretaceous Andean extensional basin. *Tectonophysics* 313, 433–447.
- April, R., Newton, R., Coles, L.T., 1986. Chemical weathering in two Adirondack watersheds: past and present day rates. *Geol. Soc. Am. Bull.* 97, 1232–1238.
- Arnold, M., Merchel, S., Bourlès, D.L., Braucher, R., Benedetti, L., Finkel, R.C., Aumaître, G., Gottang, A., Klein, M., 2010. The French accelerator mass spectrometry facility ASTER: improved performance and developments. *Nucl. Instrum. Methods Phys. Res., Sect. B* 268, 1954–1959.
- Bazilevskaya, E., Lebedeva, M., Pavich, M., Rother, G., Parkinson, D.Y., Cole, D., S.L., B., 2013. Where fast weathering creates thin regolith and slow weathering creates thick regolith. *Earth Surf. Process. Landf.* 38, 847–858. <http://dx.doi.org/10.1002/esp.3369>.
- Beaulieu, C., Sarmiento, J.L., Mikaloff-Fletcher, S.E., Chen, J., Medvigy, D.J., 2012. Identification and characterization of abrupt changes in the land uptake of carbon. *Glob. Biogeochem. Cycles* 26, GB1007. <http://dx.doi.org/10.1029/2010GB004024>.
- Bern, C.R., Thompson, A., Chadwick, O.A., 2015. Quantification of colloidal and aqueous element transfer in soils: the dual-phase mass balance model. *Geochim. Cosmochim. Acta* 151, 1–18.
- Berner, R., 1978. Rate control of mineral dissolution under earth surface conditions. *Am. J. Sci.* 278, 1235–1252.
- Berner, R., 1981. Kinetics of weathering and diagenesis. In: Lasaga, A., Kirkpatrick, R. (Eds.), *Kinetics of Geochemical Processes/Reviews in Mineralogy 8*. Mineralogical Society of America, Washington, D.C., pp. 111–134.
- Berner, R.A., Holdren, G.R., 1977. Mechanism of feldspar weathering. Some observational evidence. *Geology* 5, 369–372.
- Berner, R.A., Holdren, G.R., 1979. Mechanism of feldspar weathering. 2. Observations of feldspars from soils. *Geochim. Cosmochim. Acta* 43, 1173–1186.
- Borde, J., 1966. *Les Andes de Santiago et Leur Avant-Pays: Etude de Géomorphologie*. Union Fr. d'Impression, Bordeaux, France (559 pp.).
- Brantley, S.L., White, A.F., 2009. Approaches to modeling weathered regolith. *Reviews in Mineralogy and Geochemistry*. Mineralogical Society of America, pp. 435–484.
- Brantley, S.L., Crane, S.R., Crerar, D.A., Hellmann, R., Stallard, R., 1986. Dissolution at dislocation etch pits in quartz. *Geochim. Cosmochim. Acta* 50, 2349–2361.
- Braucher, R., Brown, E.T., Bourlès, D.L., Colin, F., 2003. In situ produced ¹⁰Be measurements at great depths: implications for production rates by fast muons. *Earth Planet. Sci. Lett.* 211, 251–258.
- Braun, J.J., Marechal, J.C., Riotte, J., Boeglin, J.L., Bedimo, J.P.B., Ngoupayou, J.R.N., Nyeck, B., Robain, H., Sekhar, M., Audry, S., Viers, J., 2012. Elemental weathering fluxes and saprolite production rate in a Central African lateritic terrain (Nsimi, South Cameroon). *Geochim. Cosmochim. Acta* 99, 243–270.
- Brimhall Jr., G.H., Dietrich, W.E., 1987. Constitutive mass balance relations between chemical-composition, volume, density, porosity, and strain in metasomatic hydrochemical systems—results on weathering and pedogenesis. *Geochim. Cosmochim. Acta* 51, 567–587.
- Brimhall, G.H., Lewis, C.J., Ford, C., Bratt, J., Taylor, G., Warin, O., 1991. Quantitative geochemical approach to pedogenesis: Importance of parent material reduction, volumetric expansion, and eolian influx in lateritization. *Geoderma* 51, 51–91.
- Brüggen, H., 1950. *Fundamentos de la Geología de Chile*. Inst. Geogr. Mil, Santiago (510 pp.).
- Burkins, D.L., Blum, J.D., Brown, K., Reynolds, R.C., Erel, Y., 1999. Chemistry and mineralogy of a granitic, glacial soil chronosequence, Sierra Nevada Mountains, California. *Chem. Geol.* 162, 1–14.
- Buss, H.L., Sak, P.B., Webb, S.M., Brantley, S.L., 2008. Weathering of the Rio Blanco quartz diorite, Luquillo Mountains, Puerto Rico: coupling oxidation, dissolution, and fracturing. *Geochim. Cosmochim. Acta* 72, 4488–4507.
- Casanova, M., Salazar, O., Seguel, O., Luzio, W., 2013. *The Soils of Chile*. World Soils Book Series/Springer Science + Business Media, Dordrecht (185 pp.).
- Chmieleff, J., von Blanckenburg, F., Kossert, K., Jakob, D., 2009. Determination of the ¹⁰Be half-life by multi-collector ICP mass spectrometry and liquid scintillation counting. *Geochim. Cosmochim. Acta* 73 (Suppl. 1), A221 (2009 Goldschmidt Conference).
- Colin, F., Alarçon, C., Vieillard, P., 1993. Zircon: an immobile index in soils? *Chem. Geol.* 107, 273–276.
- Cornu, S., Lucas, Y., Lebon, E., Ambrosi, J.P., Luizão, F., Rouiller, J., Bonnay, M., Neal, C., 1999. Evidence of titanium mobility in soil profiles, Manaus, central Amazonia. *Geoderma* 91, 281–295.
- Encinas, A., Maksaev, V., Pinto, L., Le Roux, J.P., Munizaga, F., Zentilli, M., 2006. Pliocene lahar deposits in the Coastal Cordillera of central Chile: implications for uplift, avalanche deposits, and porphyry copper systems in the main Andean Cordillera. *J. S. Am. Earth Sci.* 20, 369–381.
- Farias, M., Charrier, R., Carretier, S., Martinod, J., Fock, A., Campbell, D., Caceres, J., Comte, D., 2008. Late Miocene high and rapid surface uplift and its erosional response in the Andes of central Chile (33°–35°S). *Tectonics* 27, TC1005. <http://dx.doi.org/10.1029/2006TC002046>.
- Fletcher, R.C., Buss, H.L., Brantley, S.L., 2006. A spheroidal weathering model coupling porewater chemistry to soil thicknesses during steady-state denudation. *Earth Planet. Sci. Lett.* 244, 444–457.
- Garreaud, R.D., 2009. The Andes climate and weather. *Adv. Geosci.* 7, 1–9.
- Graham, R.C., Franco-Vizcaino, E., 1992. Soils on igneous and metavolcanic rocks in the Sonoran Desert of Baja California, Mexico. *Geoderma* 54, 1–21.
- Graham, R.C., Guertal, W.R., Tice, K.R., 1994. *The Pedologic Nature of Weathered Rock*. Whole Regolith Pedology: Soil Science Society of America Special Publication 34. Soil Science Society of America, Madison, WI, pp. 21–40.
- Jin, L., Ravella, R., Ketchum, B., Bierman, P.R., Heaney, P., White, T., Brantley, S.L., 2010. Mineral weathering and elemental transport during hillslope evolution at the Susquehanna/Shale Hills Critical Zone Observatory. *Geochim. Cosmochim. Acta* 74, 3669–3691.
- Juez-Larré, J., Kukowski, N., Dunai, T.J., Hartley, A.J., Andriessen, P.A.M., 2010. Thermal and exhumation history of the Coastal Cordillera arc of northern Chile revealed by thermochronological dating. *Tectonophysics* 495, 48–66.
- Kamei, A., Fukushi, K., Takagi, T., 2012. Chemical overprinting of magmatism by weathering: a practical method for evaluating the degree of chemical weathering of granitoids. *Appl. Geochem.* 27, 796–805.
- Kump, L.R., Brantley, S.L., Arthur, M.A., 2000. Chemical weathering, atmospheric CO₂, and climate. *Annu. Rev. Earth Planet. Sci.* 28, 611–667.
- Kurtz, A.C., Derry, L.A., Chadwick, O.A., Alfano, M.J., 2000. Refractory element mobility in volcanic soils. *Geology* 28, 683–686.
- Lal, D., 1991. Cosmic ray labeling of erosion surfaces: In situ nuclide production rates and erosion models. *Earth Planet. Sci. Lett.* 104, 424–439.
- Larson, R.L., Pitman, W.C., 1972. World-wide correlation of Mesozoic magnetic anomalies and its implications. *Bull. Geol. Soc. Am.* 83, 3645–3661.
- Lasaga, A., Blum, A., 1986. Surface chemistry, etch pits and mineral water reactions. *Geochim. Cosmochim. Acta* 50, 2363–2379.
- Lebedeva, M.I., Fletcher, R.C., Brantley, S.L., 2010. A mathematical model for steady-state regolith production at constant erosion rate. *Earth Surf. Process. Landf.* 35, 508–524.
- May, H.M., Acker, J.G., Smyth, J.R., Bricker, O.P., Dyar, M.D., 1995. Aqueous dissolution of low-iron chlorite in dilute acid solutions at 25 °C. *Clay Minerals* Soc. 23, 88 (abstr.).
- Middelburg, J.J., van der Weijden, C.H., Woittiez, J.R.W., 1988. Chemical processes affecting the mobility of major, minor and trace elements during weathering of granitic rocks. *Chem. Geol.* 68 (3–4), 253–273.
- Nagy, K.L., 1995. Dissolution and precipitation kinetics of sheet silicates. In: White, A.F., Brantley, S.L. (Eds.), *Chemical Weathering Rates of Silicate Minerals*. Mineral. Soc. Amer. Short Course 31. MSA, pp. 173–234.
- National Irrigation Commission, 1998. *Estudio integral de riego proyecto de aprovechamiento de aguas servidas planta de tratamiento Santiago Sur, Región Metropolitana*. Volumen 1.
- Nesbitt, H.W., 1979. Mobility and fractionation of rare earth elements during weathering of a granodiorite. *Nature* 279 (5710), 206–210.
- Nesbitt, H.W., Young, G.M., 1982. Early Proterozoic climates and plate motions inferred from major element chemistry of lutites. *Nature* 299, 715–717.
- Nesbitt, H.W., Markovics, G., Price, R.C., 1980. Chemical processes affecting alkalis and alkaline earths during continental weathering. *Geochim. Cosmochim. Acta* 44, 1659–1666.
- Pankhurst, R.J., Hole, M.J., Brook, M., 1988. Isotope evidence for the origin of Andean granites. *Trans. R. Soc. Edinb. Earth Sci.* 79, 13–133.
- Parada, M., Féraud, G., Fuentes, F., Aguirre, L., Morata, D., Larrondo, P., 2005. Ages and cooling history of the Early Cretaceous Caleu pluton: testimony of switch from a rifted to a compressional continental margin in central Chile. *J. Geol. Soc. Lond.* 162, 273–287.
- Pichowiak, S., 1994. Early Jurassic to early Cretaceous magmatism in the Coastal Cordillera and the Central Depression of North Chile. In: Reutter, K.J., Scheuber, E., Wigger, P.J. (Eds.), *Tectonics of the Southern Central Andes*. Springer-Verlag, Berlin, pp. 203–217.
- Riebe, C.S., Kirchner, J.W., Finkel, R.C., 2003. Long-term rates of chemical weathering and physical erosion from cosmogenic nuclides and geochemical mass balance. *Geochim. Cosmochim. Acta* 67, 4411–4427. [http://dx.doi.org/10.1016/S0016-7037\(03\)00382-X](http://dx.doi.org/10.1016/S0016-7037(03)00382-X).
- Rodés, A., Pallàs, R., Braucher, R., Moreno, X., Masana, E., Bourlès, D.L., 2011. Effect of density uncertainties in cosmogenic ¹⁰Be depth-profiles: dating a cemented Pleistocene alluvial fan (Carboneras Fault, SE Iberia). *Quat. Geochronol.* 6, 186–194.
- Scheuber, E., González, G., 1999. Tectonics of the Jurassic–Early Cretaceous magmatic arc of the north Chilean Coastal Cordillera (22°–26°S): a story of crustal deformation along a convergent plate boundary. *Tectonics* 18 (5), 895–910.

- Schott, J., Petit, J.C., 1987. New evidence for the mechanisms of dissolution of silicate minerals. In: Stumm, W. (Ed.), *Aquatic Surface Chemistry*. John Wiley & Sons, New York, pp. 255–292.
- Stone, J.O., 2000. Air pressure and cosmogenic isotope production. *J. Geophys. Res.* 105 (B10), 23753–23759.
- Sudom, M.D., St. Arnaud, T.J., 1971. Use of quartz, zirconium and titanium as indices in pedological studies. *Can. J. Soil Sci.* 51, 385–396.
- Taboada, T., Cortizas, A.M., García, C., García-Rodeja, E., 2006. Particle-size fractionation of titanium and zirconium during weathering and pedogenesis of granitic rocks in NW Spain. *Geoderma* 131, 218–236.
- Turner, B.F., Stallard, R.F., Brantley, S.L., 2003. Investigation of in situ weathering of quartz diorite bedrock in the Rio Icacos basin, Luquillo Experimental Forest, Puerto Rico. *Chem. Geol.* 202, 313–341.
- Walker, J.C.G., Hays, P.B., Kasting, J.F., 1981. A negative feedback mechanism for the long-term stabilisation of Earth's surface temperature. *J. Geophys. Res.* 86, 9776–9782.
- Wall, R., Gana, P., Gutiérrez, A. (1996), Mapa geológico del área de San Antonio, Map 2, 19.
- White, A.T., Blum, A.E., Schulz, M.S., Vivit, D.V., Stonestrom, D.A., Larsen, M., Murphy, S.F., Eberl, D., 1998. Chemical weathering in a tropical watershed, Luquillo Mountains, Puerto Rico: 1 long-term versus short-term weathering fluxes. *Geochim. Cosmochim. Acta* 62, 209–226.